Thermal insulation of CMAS (Calcium-Magnesium-Alumino-Silicates)- attacked plasma-sprayed thermal barrier coatings

G. Boissonnet, C. Chalk, J. Nicholls, G. Bonnet, F. Pedraza

► To cite this version:

G. Boissonnet, C. Chalk, J. Nicholls, G. Bonnet, F. Pedraza. Thermal insulation of CMAS (Calcium-Magnesium-Alumino-Silicates)- attacked plasma-sprayed thermal barrier coatings. Journal of the European Ceramic Society, 2020, 40 (5), pp.2042-2049. 10.1016/j.jeurceramsoc.2019.12.040 . hal-02542036

HAL Id: hal-02542036

https://hal.science/hal-02542036

Submitted on 14 Apr 2020

Thermal insulation of CMAS (Calcium-Magnesium-Alumino-Silicates)-attacked plasma-sprayed thermal barrier coatings

G. Boissonnet*[1], C. Chalk[2], J. Nicholls[2], G. Bonnet[1], F. Pedraza[1]

1. Université de La Rochelle, Laboratoire des Sciences de l'Ingénieur pour l'Environnement (LaSIE UMR-7356 CNRS), Avenue Michel Crépeau, 17042 La Rochelle, cedex 01 – France.

2. Cranfield University, Surface Engineering and Nanotechnology Institute (SENTi), College Rd, Wharley End, Bedford MK43 0AL – United Kingdom.

*corresponding author: germain.boissonnet@univ-lr.fr

Abstract. The impact of the penetration of small quantities of calcium-magnesium-alumino-silicates (CMAS) glassy melt in the porous plasma-sprayed (PS) thermal barrier coatings (TBCs) is often neglected even though it might play a non-negligible role on the sintering and hence on the thermal insulation potential of TBCs. In this study, the sintering potential of small CMAS deposits (from 0.25 to 3 mg.cm^{-2}) on freestanding yttria-stabilized zirconia (YSZ) PS TBCs annealed at 1250°C for 1 h was investigated. The results showed a gradual in-depth sintering with increasing CMAS deposits. This sintering was concomitant with local transformations of the tetragonal YSZ and resulted in an increase in the thermal diffusivity of the coatings that reached a maximum of ~110 % for the fully penetrated coating.

1. Introduction

Among the different sources of identified failures of yttria-stabilized zirconia (YSZ) -based thermal barrier coatings (TBCs) of fuel-fired engines [1], the infiltration of siliceous molten deposits, also known as Calcium-Magnesium-Alumino-Silicates (CMAS) is of growing concern [2]. In the hot-gas path and at peak temperatures, CMAS deposits yields a glassy melt that can penetrate the porous structure of ceramic coatings due to their low viscosity [3, 4]. Infiltration of the CMAS melt in the void spaces of the coating leads to sintering of this porous structure. Sintering of the ceramic is known to reduce the TBC mechanical performances [5, 6, 7] but may also contribute to a decrease in thermal resistance due to the loss of phonon-scattering defects, i.e. microcracks or lamellar interspaces of plasma sprayed TBCs [8, 9, 10]. However, only few studies proved this CMAS-sintering to result in a decline of the insulation capacity of TBCs [11, 12]. In addition to sintering, the penetrated melt can chemically attack the insulating oxide through a dissolution-reprecipitation mechanism that induces the destabilization of the t' phase, desirable for toughness [13, 14]. Such destabilization results from depletion of Y in the ceramic matrix, which may generate an increase in heat transport since the thermal conductivity of YSZ is dependent of the Y content [15].

The low-melting temperature of these silicate deposits (around 1200°C [2]) is therefore becoming a fundamental barrier to the increase of the gas temperature and reduction of fuel consumption, hence on the engine efficiency. Thus, a full understanding of the impact that CMAS can exert on the insulating properties of TBCs is of crucial importance.

Kakuda et al. investigated the effect of amorphous CMAS infiltration on the thermal properties and heat transport of plasma-sprayed (APS) coatings using photothermal emission analysis (PopTea) and observed a rise in both volumetric heat capacity and thermal conductivity of the coating upon infiltration [12]. However, the study focused only on a fully-infiltrated coating using an excess of one composition of CMAS. Previous studies have demonstrated the importance of the CMAS composition on the characteristics and severity of the attack, due to the basicity of the oxide melt [16]. For instance, the presence of iron oxide Fe_2O_3 led to a decrease of the melting point via the formation of eutectics [17], hence reducing the viscosity of the melt, which in turn induced a faster penetration of the CMAS [18].

Therefore, this investigation intended to shed light on the influence of the amount of CMAS on the thermal conductivity of YSZ TBCs. The study focused on finding the onset quantity of CMAS likely to induce enough changes to alter the thermal conductivity of the coatings. Small amounts of CMAS were deposited on the surface of plasma-sprayed coatings followed with a high temperature heat treatment for infiltration to occur. Laser-flash analysis (LFA), differential scanning calorimetry (DSC) and density measurements were conducted to measure the changes in the thermal properties of the coatings induced by CMAS infiltrations.

2. Experimental methods

The coatings considered in this study were produced by SR Technics Airfoil Services, Ltd. (Ireland) on Inconel 600 (15.5 Cr, 8.0 Fe, 0.5 Mn, < 0.5 Cu, < 0.5 Si, wt. %, bal. Ni) substrates. The thermal barrier coating systems comprised a ~300 µm plasma-sprayed YSZ coating deposited on top of a ~70 µm plasma-sprayed NiCrAlY bond coating (***Fig. 1***). The samples were prepared with a square shape (10 x 10 mm^2) for the laser flash measurements.

The CMAS mixture, whose composition is given in ***Table 1*** was used for the corrosion tests. This composition was drawn from previous studies conducted by Aygun et al. [13] and is close to the model CMAS composition used in other studies [2]. The individual oxide powders were mixed in deionized water to form a thick paste that was put into Pt-10Rh crucibles and heated a first time at 1400°C for 4 h. The resulting glassy melt was crushed in a mortar, re-melted for 4 h at 1400°C to improve the glass homogeneity and crushed again.

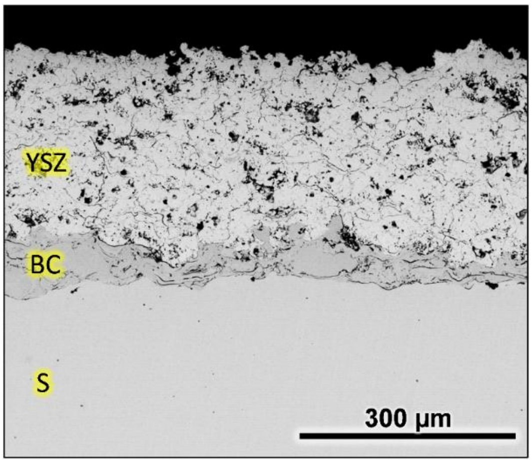

NB: YSZ = ceramic; BC = bond coating; S = substrate

Fig. 1 *– BSE micrographs of the as-deposited plasma-sprayed YSZ coating.*

Table 1 *– Average composition of the model CMAS measured via EDS (mol. %).*

CaO	MgO	Al_2O_3	SiO_2	Fe_2O_3
36	6	5	52	1

The resulting powders were mixed with milliQ water to a 50/50 weight ratio before spraying on the samples using an air brush. The samples to coat were weighed using a 10^{-5} g precision balance prior to CMAS deposition. Then, the samples were pre-heated at 80°C to help the adhesion of the CMAS by evaporating the water once the spray in contact with the surface of the sample. Thus, short spray pulses were successively applied with intermediate re-heating and weighing of the samples till the desired mass of deposited CMAS was obtained.

First, tests were conducted to investigate the kinetics of penetration of the CMAS melt into the coatings. Therefore, thick deposits of ~20 mg.cm^{-2} were applied on the surface of plasma-sprayed TBC and different durations of heat treatment were investigated. The samples were placed in a furnace at room temperature and heated to 1250°C (above the melting point of the mixture as observed by DSC), and removed after 15 and 30 min, 1 and 2 h. ***Fig. 2*** shows that after only 15 minutes, and despite a non-homogeneous front, the CMAS has almost sintered 200 µm of the YSZ coating (up to the red line) by infiltration through the pores. Moreover, the CMAS melt started to saturate the TBC (blue region) through the dissolution of the YSZ material, hence resulting in the loss of the initial microstructure of the coating. Therefore, smaller quantities were investigated using the 1 h heat treatment to isolate the sintering effect of the CMAS from this type of excessive degradation.

Freestanding coatings were used in this study to isolate their contribution to the heat transport from the whole system. The freestanding coatings were obtained by chemically dissolving the oxide interface between the bond coating and the YSZ TBC in a 20 vol. % HCl aqueous solution. CMAS deposits of 0.25, 0.50, 1 and 3 mg.cm^{-2} were applied on the freestanding coatings which were then placed in a muffle furnace pre-heated at 1250°C. After 1 h of annealing, the samples were removed from the furnace and quenched in air at room temperature.

The microstructural changes were investigated in polished cross-sections with a FEI Quanta 200F scanning electron microscope (SEM) coupled to an EDAX detector for local analysis of the composition using energy dispersive spectrometry (EDS). X-ray diffraction (XRD, Brüker AXS D8 Advance) using the λ_{Cu} in θ-2θ mode and Raman micro-spectrometry (Jobin Yvon LabRam HR800, λ_{laser} ~632nm) were employed to follow the change in structure of the ceramic coatings, respectively, on the surface and on the cross-section of the coatings.

The phase structures were examined by X-ray diffraction technique using Rietveld refinement technique. The mole percentages of monoclinic phase M_m, tetragonal phase $M_{t'/t}$ and cubic phase M_c were obtained from the following equations [20]:

$$\frac{M_m}{M_{t'/t,c}} = 0.82\frac{I_m(\bar{1}11) + I_m(111)}{I_{t'/t,c}(111)} \tag{1}$$

$$\frac{M_c}{M_{t'/t}} = 0.88\frac{I_c(400)}{I_{t'/t}(400) + I_{t'/t}(004)} \tag{2}$$

Where $I_m(\bar{1}11)$ and $I_m(111)$ are the integral net intensities for monoclinic phase reflected from $(\bar{1}11)$ and (111) peaks; and $I_{t'/t,c}(111)$ is the intensity for tetragonal or cubic phase reflected from (111) plane. $I_c(400)$ is the intensity for cubic phase reflected from (400) plane. $I_{t'/t}(400)$ and $I_{t'/t}(004)$ are the intensities for tetragonal phase reflected from (400) and (004) plane, respectively.

To assess the evolution of the thermal insulation potential of the TBCs, thermal diffusivity was determined using high-temperature laser-flash measurements with a Linseis LFA1600 apparatus at low pressure (~1.10^{-2} mbar) every 100°C between room temperature and 1100°C. Three samples for the same deposited quantity of CMAS were analyzed with five separate laser shots per sample at each temperature step to increase the accuracy of the results.

The thicknesses of the multilayer samples were determined (±10^{-3} mm) with a digital caliper prior to the laser flash measurements. All samples were also coated on both sides with gold (thin sputtering) and graphite (2 µm / side) to increase the absorption and the emissivity of the laser shot through the sample. One shall consider that the graphite deposits may alter the actual inherent thermal diffusivity values, but the protocol employed in all our study allows a direct comparison of the different CMAS attacked TBCs.

3. Results

3.1. Transformations due to CMAS penetration

3.1.1. With 20 mg.cm^{-2} deposits

Fig. 2 shows the depth of penetration of the CMAS melt for different times of annealing at 1250°C. The CMAS melt penetrated quite rapidly with a non-homogeneous front into the porous network of the coatings. Indeed, almost 200 µm were completely sintered (up to the red line) after only 15 minutes. Moreover, it is observed that significant transformations of the initial microstructure occurred by the appearance of round-shaped pores and CMAS-saturated zones (blue region).

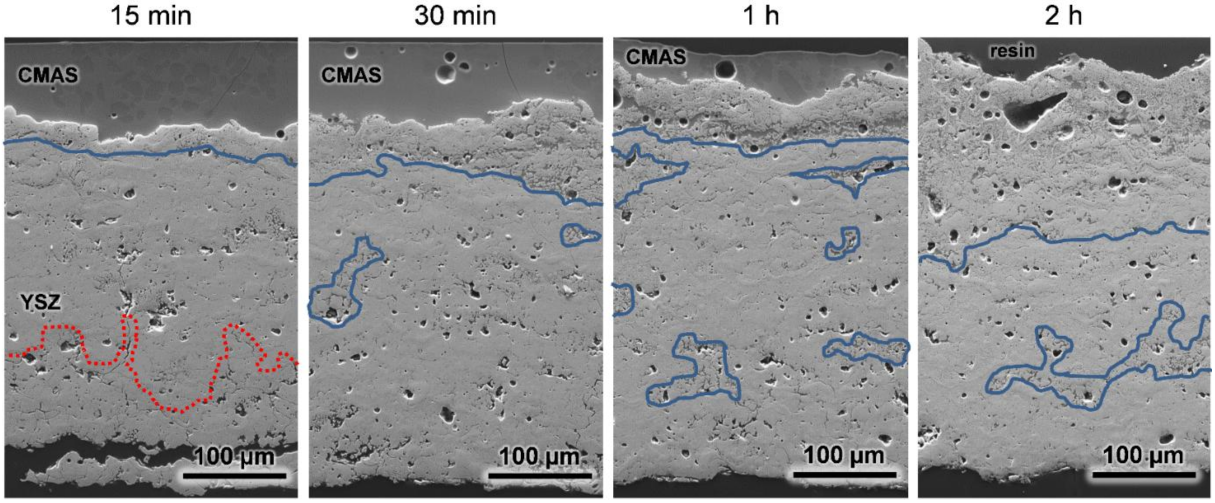

Fig. 2 *– BSE micrographs of plasma-sprayed YSZ coatings annealed at 1250°C for different times with CMAS deposits of 20 mg.cm^{-2}.*

The evolution of the different phases was evaluated at local scale by Raman spot analyses (***Fig. 3***). The tetragonal (t+t') and the monoclinic phases of zirconia were unambiguously differentiated in the as-deposited and upon exposure to CMAS. While the distribution of the tetragonal phases is quite even across the coatings' thickness, the appearance of the monoclinic phase appears more random while intense. However, the occurrence and intensity of the monoclinic doublets (175 and

200 cm^{-1} A_g vibrational modes) increase with exposure time, in particular in the upper zone of the coatings which is saturated with CMAS. This clearly indicates that either the amount and/or the time of exposure to CMAS may induce phase transformations of the YSZ.

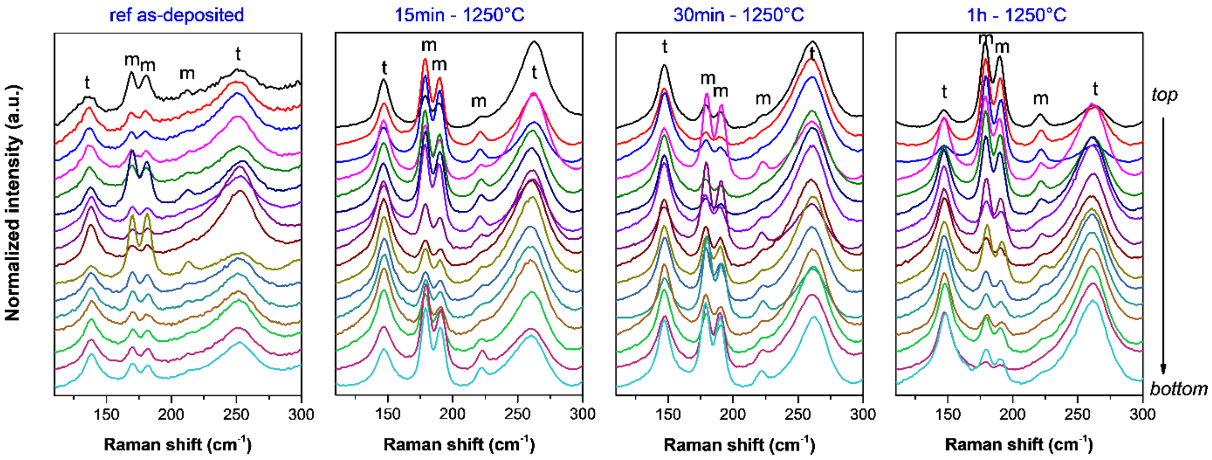

Fig. 3 – Raman local spot analysis of plasma-sprayed YSZ coatings annealed at 1250°C for different times with CMAS deposits of 20 mg.cm^{-2}.

3.1.2. With 0.25, 0.50, 1 and 3 mg.cm^{-2}

Fig. 4 shows the microstructure of the freestanding plasma sprayed coatings with CMAS deposits of 0.25, 0.5, 1 and 3 mg.cm^{-2} after annealing at 1250°C for 1h. The depth of the sintering of the porous microstructure increases (red line) with the amount of CMAS. The thin lamellar pores appear to be sintered to a depth of ~40, ~70, ~130 and ~250 µm (full depth) for, respectively, 0.25, 0.5, 1 and 3 mg.cm^{-2} of CMAS deposits. The thicker cracks and the "globular" pores remain the only porosity observed in the sintered zone affected by the CMAS. ***Fig. 5*** shows details of the microstructure of the upper (***Fig. 5***a) and lower (***Fig. 5***b) zone of the plasma coating after reaction with a deposit of 1 mg.cm^{-2} of CMAS and annealed at 1250°C for 1 h. The microstructure of the upper part of the coating that has been mostly exposed to the CMAS melt is completely transformed. This transformed zone appears as a mixture of round shaped grains surrounded by a darker phase that comprises small bright grains in a dark matrix. The EDS spot analyses in the dark phase allowed the identification of zirconia, which is slightly depleted in Y (~8 wt.% compared to the ~9 wt.% of the measurements made on the lower part of the coating, ***Fig. 5***a), and an average of ~3 wt.% of the combined CMAS compounds. The round shaped grains were identified as zirconia with a slightly higher ratio of Y (~10 wt.%). The microstructure of the coating close to the bond coat (***Fig. 5****b*) – below the red line – is quite similar to the one of the as-deposited coating (***Fig. 1***) and presents thin cracks and globular pores.

The penetration depth of CMAS elements in the coatings as a function of initial deposited mass is given in ***Fig. 6***. These results show that the concentration of the CMAS elements into the coating decrease with increasing depth and that most of the CMAS is retained in the transformed zone above the red line of ***Fig. 4***. Moreover, the greater the amount of CMAS deposited, the higher the concentration of the CMAS compounds. It can also be noted that the concentrations of Si and of Ca decrease more rapidly than the ones of Mg, Al and Fe with depth in the coating. This suggests that the CMAS viscosity is sufficiently low to allow the percolation through the coating and that Si and Ca are likely more reactive with YSZ than Mg, Al and Fe.

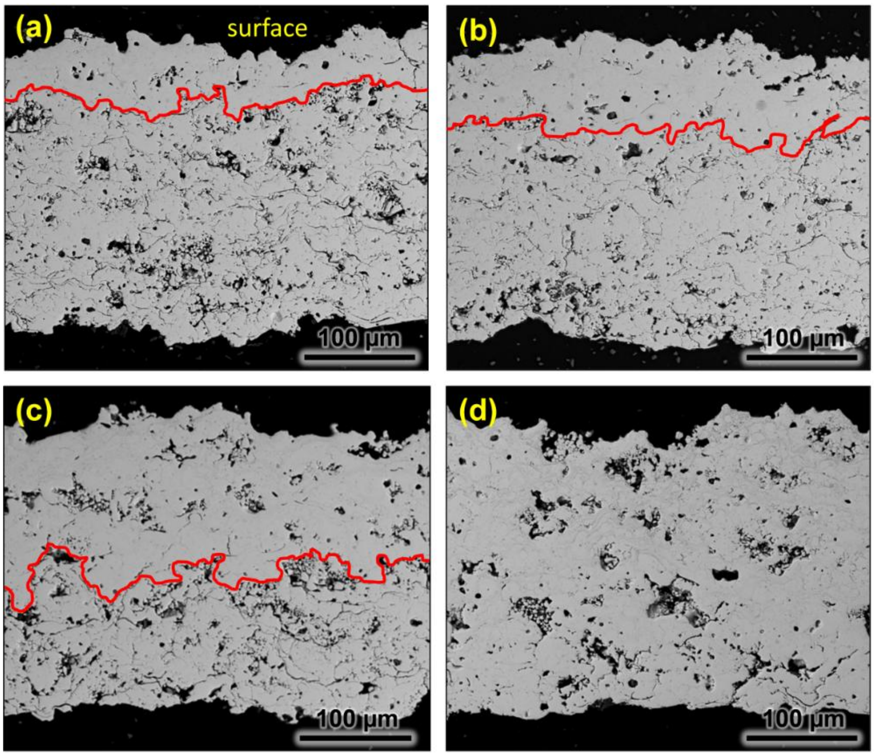

Fig. 4 *– BSE micrographs of freestanding YSZ coatings annealed at 1250°C for 1h with CMAS deposits of (a) 0.25, (b) 0.50, (c) 1.0 and (d) 3.0 mg.cm*$^{-2}$.

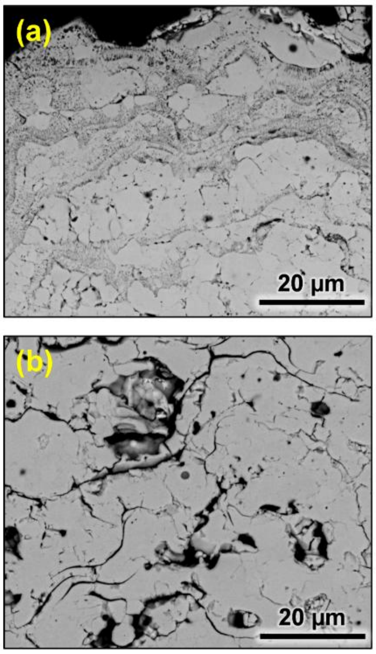

Fig. 5 *– SEM micrographs showing the microstructural differences between (a) the CMAS affected zone above the red line (see Fig. 3) and (b) the unaffected zone below the red line on the YSZ coating with CMAS deposit of 1 mg.cm^{-2} after annealing at 1250°C for 1h.*

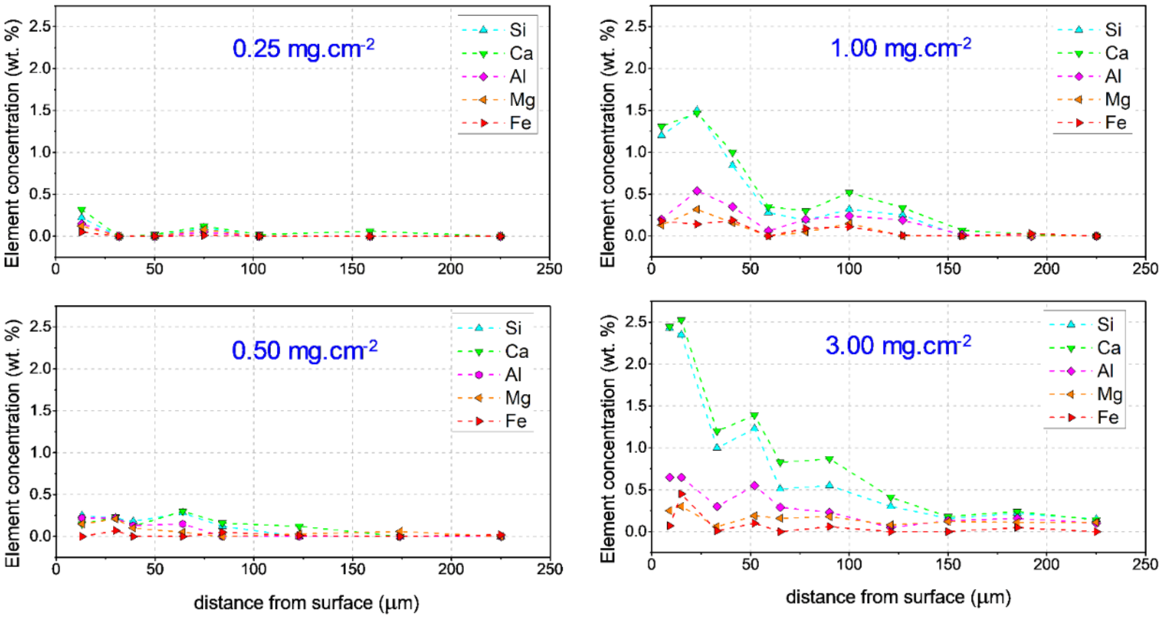

Fig. 6 *– Evolution of CMAS content with depth in the YSZ freestanding coatings for different deposited amounts.*

Fig. 7 presents the X-ray diffraction patterns for the as-deposited coating and the samples annealed at 1250°C with the different CMAS deposits. The as-deposited coating already displays the monoclinic structure of zirconia with the two peaks around 28.5° and 31.5°. Quantitative analysis using Rietveld refinement were conducted in the 27°-32° and 72°-76° ranges to identify more accurately the phase changes occurring by reaction of the YSZ with the CMAS. The results are gathered in ***Table 2***. The phase analysis shows that only the Y-rich stabilized *t'*-ZrO_2 (93.1 wt.%)

and the *m*-ZrO_2 (6.9 wt.%) are present in the as-deposited coating. The evolution of the different phases with increasing the CMAS deposits is presented on ***Fig. 8*** for a better overview. The content of *t'*-ZrO_2 tends to decrease while that of the low-yttria *t*-ZrO_2 increases with the amount of CMAS. Also, the initial *m*-ZrO_2 phase content decreases with annealing, but then, follows a slight increasing trend with the amount of CMAS. In contrast, the *c*-ZrO_2 phase appears after annealing but once formed, its content is similar irrespective of the CMAS amount. These results indicate that yttria is depleted from the zirconia with the increasing additions of CMAS.

The evolution of the different phases was also evaluated at local scale by Raman spot analyses. The results are presented in ***Fig. 9***. In contrast with the results obtained with the 20 mg.cm^{-2} of CMAS deposit, the Raman spectra highlight the progressive homogenisation of the *m*-ZrO_2 phase content as the CMAS melt penetrates the coating with increasing the amount of CMAS; these results being consistent with the ones of XRD (***Fig. 8***).

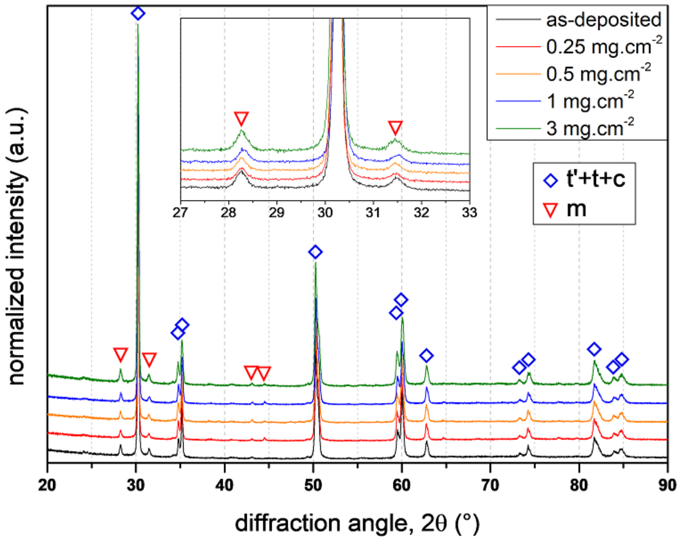

Fig. 7 *– XRD patterns of the CMAS-attacked freestanding YSZ coatings compared with the as-deposited one.*

Table 2 *– Relative percentages and yttria contents for zirconia phases in as-sprayed and in CMAS attacked YSZ coatings (Rietveld analysis).*

Sample	***c*-ZrO_2** (wt.%)	Yttria content (wt.%)	***t'*-ZrO_2** (wt.%)	Yttria content (wt.%)	***t*-ZrO_2** (wt.%)	Yttria content (wt.%)	***m*-ZrO_2** (wt.%)
as-deposited	-	-	93.1	7.3	-	-	6.9
0.25	1.8	9.1	82.9	7.4	12.3	5.6	3.0
0.50	1.3	9.0	81.8	7.3	13.7	5.6	3.2
1	1.0	10.8	77.9	7.5	18.0	5.3	3.1

3	1.6	10.9	65.0	7.5	28.6	5.2	4.8

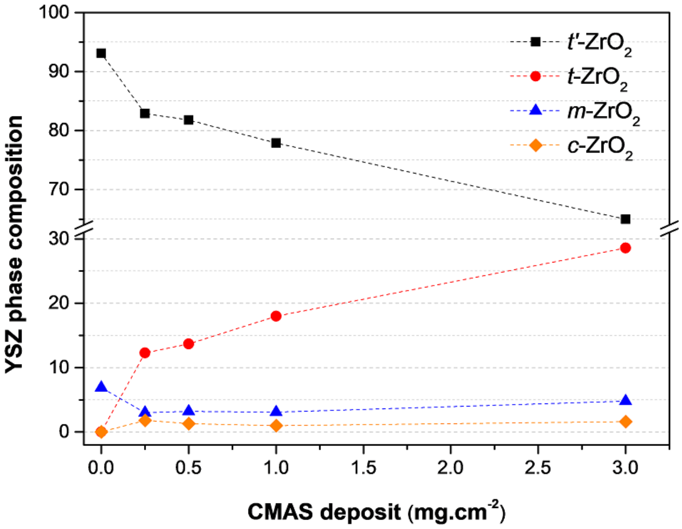

Fig. 8 *– Evolution of the different phase percentage in CMAS-attacked YSZ coatings.*

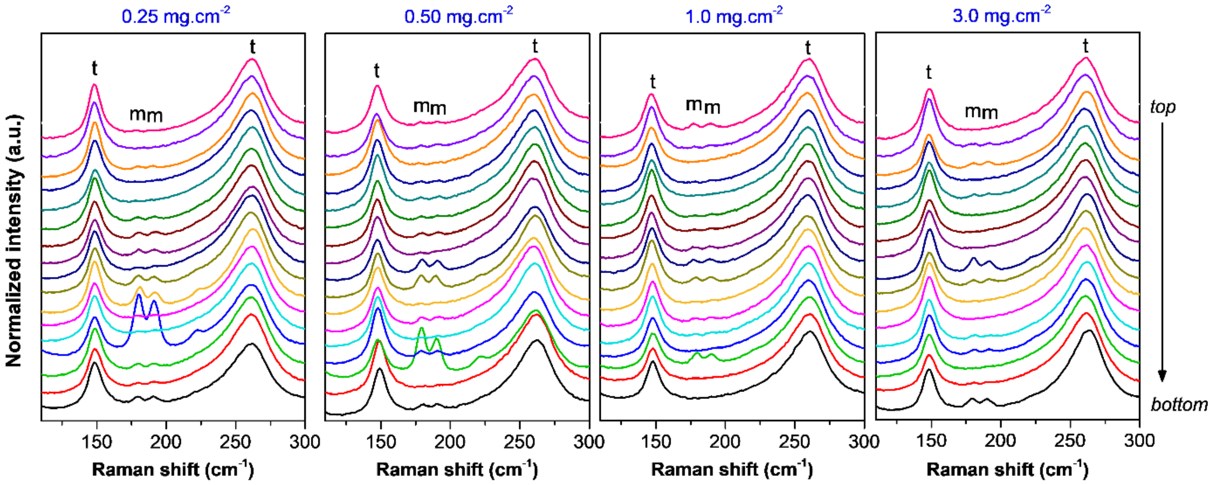

Fig. 9 *– Local Raman spot analysis of the CMAS-attacked freestanding YSZ coatings.*

3.2. Thermal diffusivity

The thermal diffusivity as a function of the temperature for the as-deposited coatings and for the annealed samples (with and without CMAS deposits) is presented on ***Fig. 10***. The as-deposited coating displays a thermal diffusivity comprised between 4.10^{-7} (at RT) and 3.10^{-7} $m^2.s^{-1}$ (at 1000°C) with a minimum observed at 600°C. The values raise to 6.10^{-7} (RT) and 4.10^{-7} $m^2.s^{-1}$ (1000°C) when annealed at 1250°C for 1 h without CMAS. In the presence of CMAS, the thermal diffusivity increases gradually with increasing the amount of CMAS. The effect of the deposited amount of CMAS on the thermal diffusivity is plotted in ***Fig. 11***. With respect to the annealed and CMAS-free coatings, the thermal diffusivity of the CMAS-attacked layers increases by ~15, ~30, ~50 and 110 % for, respectively, the 0.25, 0.5, 1 and 3 $mg.cm^{-2}$ amounts of CMAS. One can assume a parabolic relationship between the CMAS deposited quantity and the observed rise in thermal diffusivity. This tendency was observed as the thickness affected by the melt also followed a similar relationship with the deposited amount of CMAS (see ***Fig. 12***).

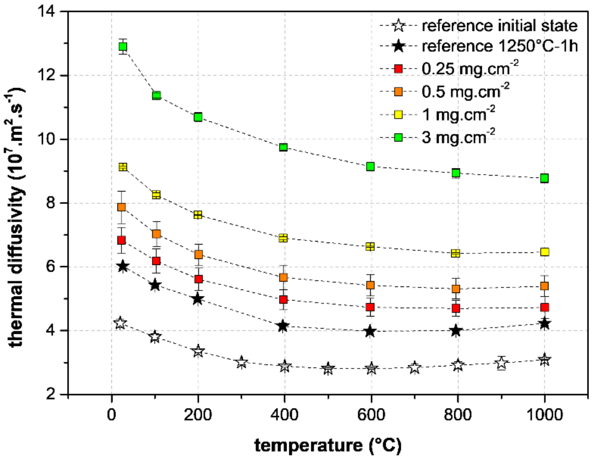

Fig. 10 *– Thermal diffusivity of the CMAS-attacked freestanding YSZ coatings compared with the as-deposited reference with and without annealing at 1250°C for 1h.*

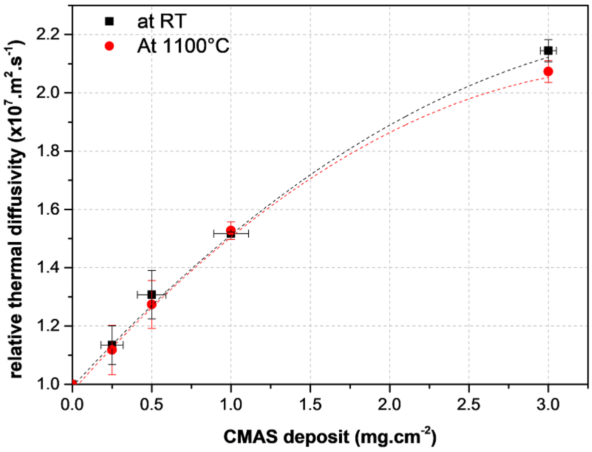

Fig. 11 *– Relative thermal diffusivity of the freestanding YSZ coatings annealed at 1250°C for 1h with CMAS deposits of 0.25, 0.50, 1.0 and 3.0 mg.cm*$^{-2}$*.*

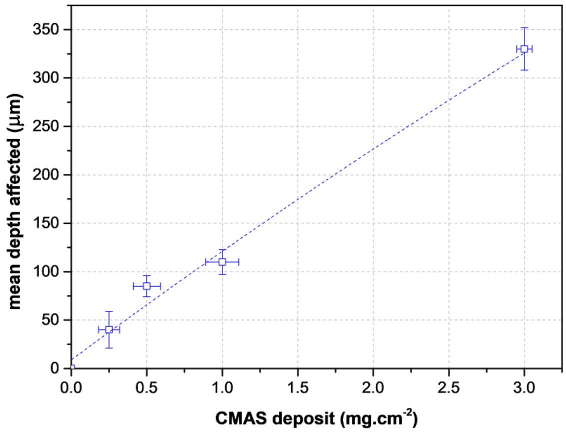

Fig. 12 *– Mean depth of the CMAS penetration in the freestanding YSZ coatings (measured by image analysis) as a function of the deposited quantity after annealing at 1250°C for 1h.*

Fig. 13 gives the lamellar porosity level as well as the thermal diffusivity at room temperature of the freestanding coatings in the as-deposited and in the annealed conditions. The data are compared with other similar freestanding coatings measured in a previous study [21]. The as-deposited coatings display a lamellar porosity rate of ~11.7% for a thermal diffusivity at room temperature of ~4.2.10^{-7} m^{2}.s^{-1}. The annealing treatment of 1 h at 1250°C performed in this study leads to a lamellar porosity rate of ~9.5%, which is similar to the one obtained in a previous study after 50h at 1150°C [21]. The resulting thermal diffusivity at RT of both annealed coatings is also observed to be similar (~6.10^{-7} m^{2}.s^{-1}). Finally, one should note that the lamellar porosity level measured in the unaffected zone of the coatings annealed with 1 mg.cm^{-2} CMAS (see ***Fig. 5***b) is close to the one of the annealed coating without CMAS (~9.6%). In the CMAS-attacked zone, the thin lamellar porosity disappeared with only the larger cracks and globular pores remaining and hence, a lamellar porosity value of 0% was attributed to this zone.

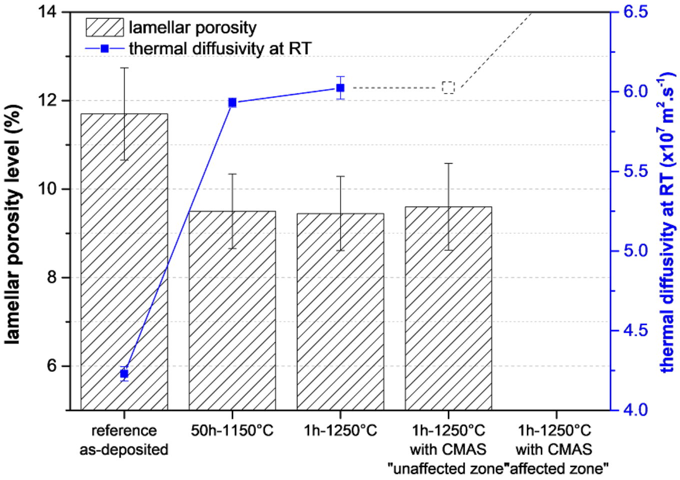

Fig. 13 – *Lamellar porosity levels of the PS coatings of the study compared with the one of the same coatings measured in [21] versus the thermal diffusivity measured at room temperature. Dash line relate to hypothetic thermal diffusivity values.*

4. Discussion

The penetration of the CMAS melt has been shown to be associated with the loss of the initial microstructure of the coatings that resulted in closure of the thin pores and appearance of round-shaped pores (***Fig. 2***). This transformation results from the dissolution-reprecipitation mechanism described in numerous studies [2, 3, 14]. The appearance of round shaped pores, once reported by Borom et al. [3] is a frothing phenomenon, the origin of which is still under debate. Li et al. ascribed the froth to the fact that the air within the porous coating structure tries to escape from it and is trapped within the molten phase [22]. This phenomenon was observed for the substantial deposits of 20 mg.cm^{-2} and in other studies that employed large amounts of CMAS deposits [3, 11, 22]. However, no evidence of frothing was observed with the smaller deposits of 0.25 to 3 mg.cm^{-2} (***Fig. 4***). This means that, when using smaller amounts of deposited CMAS, the melt is not significant enough to create a large melted zone via dissolution of the YSZ material.

The microstructure of the “affected” zone in the case of the small deposits (***Fig. 5a***) looks like the one observed in other studies [3, 11, 13]. After the dissolution of the *t’*-ZrO_2 in the CMAS melt, the zirconia reprecipitates into round-shaped grains that are either depleted in yttria and transformed to monoclinic on cooling, or enriched in Y and fully stabilised into *c*-ZrO_2 [14]. The Y-depletion was ascribed to the higher solubility of Y^{3+} in the glassy melt compared to Zr^{4+} ions that leads to further reprecipitation of *m*-ZrO_2 [14]. The higher content of Y that was measured via EDS in the round shaped grains of zirconia (see ***Fig. 5a***) could be linked to a possible enrichment in Y during reprecipitation, leading to a partial transformation of the *t’*-ZrO_2 into a *c*-ZrO_2 [14], which is also in line with our XRD results (see **Table 2**). For instance, Kramer et al. identified via TEM and EDS analysis the globular grains to be made of *c*-ZrO_2 surrounded by a mixture of crystallized aluminium silicates and residual glassy CMAS (the dark matrix of ***Fig. 5a***) in which small grains of zirconia were embedded [14, 24]. The darker phase in the “affected” zone of ***Fig. 5a*** would thus be composed of reprecipitated small grains of Y-lean zirconia in the anorthite ($Ca_2ZrSi_4O_{12}$) matrix often reported in other studies with similar CMAS compositions [2, 19]. One should note that in this study the deposited amounts of CMAS are very small compared to those of other works. Therefore, the CMAS becomes the limiting reagent in our case and different reaction products than those reported may also form. In addition, as opposed to the significant increase of the *m*-ZrO_2 observed for the substantial CMAS deposits of 20 $mg.cm^{-2}$ (***Fig. 3***), the X-ray analysis and the Raman spectra of the coatings with the small deposits (***Table 2*** and ***Fig. 9***) show a decrease of the *t’*-ZrO_2 associated with an increase of the *t*-ZrO_2 while the *m*-ZrO_2 slightly decrease with the annealing and then slowly increase with increasing the amount of CMAS. The formation of the *m*-ZrO_2 may be impeded upon quenching (see the $YO_{1.5}$–ZrO_2 phase diagram **Fig. 14**), which would agree with the opinion of Aygun et al. [19]. However, as the deposit of 20 $mg.cm^{-2}$ led to the formation of *m*-ZrO_2, it appears more likely that the amount of deposited CMAS was not sufficient to further destabilize the *t’*-ZrO_2 into the *m*-ZrO_2 by dissolution of Y and thus resulted mostly in the formation of the Y-lean *t*-ZrO_2 instead of *m*-ZrO_2. In this sense, we have also disregarded the relatively short annealing time (1h) because we have demonstrated that, when larger quantities of CMAS were employed, transformations into *m*-ZrO_2 were possible.

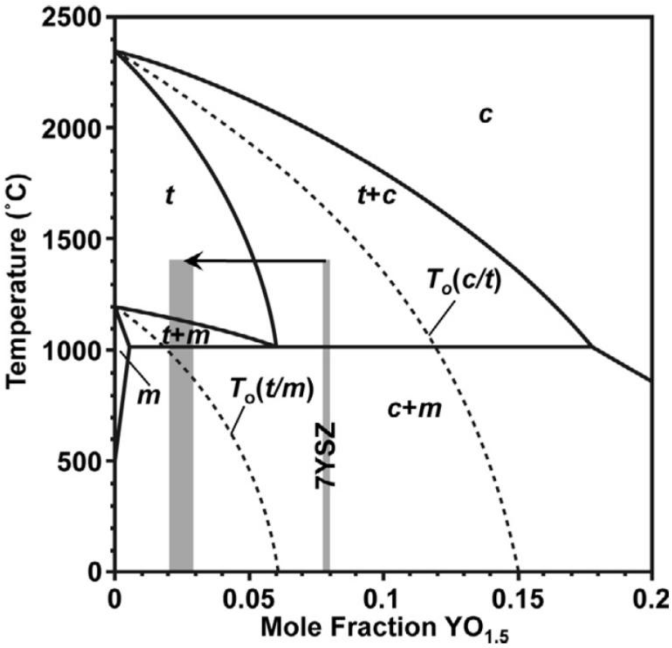

Fig. 14 *– Portion of the $YO_{1.5}$–ZrO_2 phase diagram [25]. The arrow indicates Y-depletion due to the interaction with CMAS.*

Considering the thermal diffusivity measurements (see ***Fig. 10***), it was observed that the annealing treatment at 1250°C for 1 h was already responsible for a decrease of the thermal insulation potential of the coating. This 50% rise in thermal diffusivity is very likely due to the significant sintering of the lamellar porosity of the coating that is depicted in ***Fig. 13*** and which was previously reported in similar works [10, 21]. With the addition of CMAS, the thermal diffusivity is observed to increase further. In view of the different transformations observed, the rise in the thermal diffusivity could be due to (i) the sintering of the porous structure in the "affected zone", (ii) the phase transformations described above, and (iii) the thermal properties of the CMAS itself or of the reaction products issued from the interaction between the glassy melt and the YSZ coating.

It is well-known that the reduction of the heat transport through the YSZ coating, and especially for the plasma-sprayed coatings, is mainly due to their porous network [26, 27, 28, 29]. Previous works demonstrated that sintering is a major contributor of the loss of thermal insulation potential of such coatings [10, 30, 31]. In a previous study that concerned the same freestanding coating, a reduction of the lamellar porosity rate of ~20 % led to a ~40 % increase in thermal diffusivity [21]. This means that the complete filling of the thin pores by the CMAS will result in a sintering that will increase the heat transport through the coating.

The different phase contents measured using XRD (***Table 2***) showed a significant decreasing tendency of the *t'*-ZrO_2 in favour of *t*-ZrO_2 compared with a small increase of *c*-ZrO_2 and a small decrease of *m*-ZrO_2 (see also ***Fig. 8***). Previous works also demonstrated that decreasing the Y_2O_3 content in YSZ single crystals contributed to an increase in the thermal diffusivity, i.e. a decrease from 10.6 to 7.7 wt. % resulted in an increase of the thermal diffusivity of 10% [15]. Thus, the important decrease of *t'*-ZrO_2 in favour of *t*-ZrO_2 could be responsible for further increasing the thermal diffusivity when compared to the less significant variations of the *m*-ZrO_2 and *c*-ZrO_2 phases. In addition, the phase changes measured via XRD associated with the increasing CMAS amount (***Table 2***) depend on the limited depth of penetration of the X-ray. Thus, the phase transformations depicted in ***Table 2*** relate only to a fraction of the affected depth. This would imply that the actual amount of transformed YSZ material into the less-insulating *t*-ZrO_2 might be significantly higher with increasing the deposited quantity of CMAS.

Considering the CMAS thermal properties, Kakuda et al. determined the thermal properties of amorphous and crystallized CMAS via local PopTea analysis and showed that crystallized CMAS led to very close thermal diffusivity values to that of the fully dense 7YSZ [12]. However, in the case of amorphous CMAS, the thermal diffusivity appeared to be half of the value of its crystallized form. Thus, the addition of CMAS in the coating could lead by itself to a decrease of the thermal diffusivity. However, in the coatings of this study, the CMAS retained within the coatings were estimated by EDS to be in a very small amount (see **Fig. 6**). Even in the case of the highest amount of CMAS (~3 $mg.cm^{-2}$), this mass would represent less than ~3% of the total mass of the sample and thus, the contribution of the amorphous or recrystallized phases of CMAS to the thermal properties of the sample can be disregarded.

Thus, the relatively high thermal diffusivity results for the coatings that reacted with CMAS are mostly due to the sintering effect of the CMAS melt that closed the pores, but also to the transformation of Y-rich *t'*-ZrO_2 into Y-lean *t*-ZrO_2 and *m*-ZrO_2. Moreover, one shall note that the transformations through the coatings are very heterogeneous. As a matter of fact, due to the very low viscosity of the CMAS melt, the corrosion zones are mostly located near the cracks and pores of the initial coating. This heterogeneity imply that the heat flow could be transported through preferential phases of lower resistance that forms a continuous network through the thickness of the infiltrated coatings. For instance, zircon ($ZrSiO_4$) possess a high thermal conductivity compared to zirconia, i.e. ~14 W/m.K and 3 W/m.K at 273 K for $ZrSiO_4$ and *m*-ZrO_2 respectively [32]. However, as we did not observe those phases with XRD, other local analyses are required to investigate the potential products formed and their thermal transport properties.

5. Conclusions

In this study, small quantities of CMAS were applied in order to assess the impact that the resulting partial transformation of the YSZ plasma-sprayed coating could exert on the coating thermal insulation potential. The experimental results showed a gradual increase of the sintered depth with increasing CMAS deposits accompanied by phase transformations of the YSZ. The CMAS-induced sintering and the destabilization of the *t'*-ZrO_2 were found to be the major contributions to an increase in the thermal diffusivity of the coatings; which reached a maximum of ~110 % for the fully penetrated coating.

ACKNOWLEDGEMENTS

The authors gratefully acknowledge SR Technics Airfoils Services, Ltd. (Ireland) for providing the samples of this study and the University of La Rochelle for supporting the collaboration with Cranfield University (UK).

REFERENCES

1. D.R. Clarke, M. Oechsner, N.P. Padture, *Thermal-barrier coatings for more efficient gas-turbine engines*, MRS Bulletin 37, **2012**, pp. 891-898.
2. C.G. Levi, J.W. Hutchinson, M.-H. Vidal Sétif, C.A. Johnson, *Environmental degradation of thermal-barrier coatings by molten deposits*, MRS Bulletin 37, **2012**, pp. 932-940.
3. M.P. Borom, C.A. Johnson, L.A. Peluso, *Role of environmental deposits and operating surface temperature in spallation of air plasma sprayed thermal barrier coatings*, Surface and Coatings Technology 86-87, **1996**, pp. 116-126.
4. C. Mercer, S. Faulhaber, A.G. Evans, R. Darolia, *A delamination mechanism for thermal barrier coatings subject to calcium–magnesium–alumino-silicate (CMAS) infiltration*, Acta Materialia 53, **2005**, pp. 1029-1039.
5. R.G. Wellman, J.R. Nicholls, *On the effect of ageing on the erosion of EB-PVD TBCs*, Surface and Coatings Technology 177-178, **2004**, pp. 80-88.
6. X. Zhao, X. Wang, P. Xiao, *Sintering and failure behaviour of EB-PVD thermal barrier coating after isothermal treatment*, Surface and Coatings Technology 200, **2006**, pp. 5946-5955.
7. A.C.F. Cocks, N.A. Fleck, *Constrained sintering of an air-plasma-sprayed thermal barrier coating*, Acta Materialia 58, **2010**, pp. 4233-4244.

8. I.O. Golosnoy, A. Cipitria, T.W. Clyne, *Heat transfer through plasma-sprayed thermal barrier coatings in gas turbine: a review of recent work*, Journal of Thermal Spray Technology 18, **2009**, pp. 809821.
9. L. Lu, F.-C. Wang, Z. Ma, Q.-B. Fan, *Anisotropic effect of splat interface on thermal conductivity of plasma sprayed YSZ coating*, Surface and Coatings Technology 235, **2013**, pp. 596-602.
10. H.-J. Rätzer-Scheibe, U. Schulz, *The effects of heat treatment and gas atmosphere on the thermal conductivity of APS and EB-PVD PYSZ thermal barrier coatings*, Surface and Coatings Technology 201, **2007**, pp. 7880-7888.
11. J. Wu, H.-B. Guo, Y.-Z. Gao, S.-K. Gong, *Microstructure and thermo-physical properties of yttria stabilized zirconia coatings with CMAS deposits*, Journal of the European Ceramic Society 31, **2011**, pp. 1881-1888.
12. T.R. Kakuda, C.G. Levi, T.D. Bennett, *The thermal behavior of CMAS-infiltrated thermal barrier coatings*, Surface and Coatings Technology 272, **2015**, pp. 350-356.
13. F.H. Stott, D.J. de Wet, R. Taylor, *Degradation of thermal-barrier coatings at very high temperatures*, MRS Bulletin, **1994**, pp. 46-49.
14. S. Krämer, J. Yang, C.G. Levi, *Thermochemical interaction of thermal barrier coatings with molten* $CaO–MgO–Al_2O_3–SiO_2$ *(CMAS) deposits*, Journal of the American Ceramic Society 89[10], **2006**, pp. 3167-3175.
15. J.-F. Bisson, D. Fournier, M. Poulain, O. Lavigne, R. Mévrel, *Thermal conductivity of yttria–zirconia single crystals, determined with spatially resolved infrared thermography*, Journal of the American Ceramic Society 83[8], **2000**, pp. 1993-1998.
16. M. Craig, N.L. Ndamka, R.G. Wellman, J.R. Nicholls, *CMAS degradation of EB-PVD TBCs: The effect of basicity*, Surface and Coatings Technology 270, **2015**, pp. 145-153.
17. W. Braue, P. Mechnich, Recession of an EB-PVD YSZ coated turbine blade by CaSO4 and Fe, Ti-rich CMAS-type deposits, Journal of the American Ceramic Society 94[12], **2011**, pp. 4483-4489.
18. V.L. Wiesner, U.K. Vempati, N.P. Bansal, *High temperature viscosity of calcium-magnesium-aluminosilicate glass from synthetic sand*, Scripta Materialia 124, **2016**, pp. 189-192.
19. A. Aygun, A.L. Vasiliev, N.P. Padture, X. Ma, *Novel thermal barrier coatings that are resistant to high-temperature attack by glassy deposits*, Acta Materiala 55, **2007**, pp. 6734-6745.
20. U. Schulz, *Phase Transformation in EB- PVD Yttria Partially Stabilized Zirconia Thermal Barrier Coatings during Annealing*, Journal of the American Ceramic Society 83, **2000**, pp. 904-910.

21. G. Boissonnet, G. Bonnet, A. Pasquet, N. Bourhila, F. Pedraza, *Evolution of Thermal Insulation of Plasma-Sprayed Thermal Barrier Coating Systems with Exposure to High Temperature*, accepted in Journal of the European Ceramic Society on January 14th.
22. L. Li, N. Hitchman, and J. Knapp, *Failure of Thermal Barrier Coatings Subjected to CMAS Attack*, Journal of Thermal Spray Technology 19, **2010**, pp. 148-155.
23. A.G. Evans, J.W. Hutchinson, *The mechanics of coating delamination in thermal gradients*, Surface and Coatings Technology 201, **2007**, pp. 7905-7916.
24. S. Krämer, S. Faulhaber, M. Chambers, D.R. Clarke, C.G. Levi, J.W. Hutchinson, A.G. Evans, *Mechanisms of cracking and delamination within thick thermal barrier systems in aero-engines subject to calcium-magnesium-alumino-silicate (CMAS) penetration*, Materials Science and Engineering A 490, **2008**, pp. 26-35.
25. H.F. Garces, B.S. Senturk, N.P. Padture, *In situ Raman spectroscopy studies of high-temperature degradation of thermal barrier coatings by molten silicate deposits*, Scripta Materialia 76, **2014**, pp. 29-32.
26. L.P.H. Jeurgens, W.G. Sloof, F.D. Tichelaar, E.J. Mittemeijer, *Structure and morphology of aluminium-oxide films formed by thermal oxidation of aluminium*, Thin Solid Films 418, **2002**, pp. 89-101.
27. L. Pawlowski and P. Fauchais, *Thermal Transport Properties of Thermally Sprayed Coating*, International Materials Reviews 37[6], **1992**, pp. 271-289.
28. F. Cernuschi, P. Bianchi, M. Leoni, and P. Scardi, *Thermal Diffusivity/Microstructure Relationship in Y-PSZ Thermal Barrier Coatings*, Journal of Thermal Spray Technology 8[1], **1999**, pp. 102-109.
29. I.O. Golosnoy, S.A. Tsipas, and T.W. Clyne, *An Analytical Model for Simulation of Heat Flow in Plasma Sprayed Thermal Barrier Coatings*, Journal of Thermal Spray Technology 14[2], **2005**, pp. 205-214.
30. F. Cernushi, L. Lorenzoni, S. Ahmaniemi, P. Vuoristo, and T. Mäntylä, *Studies of the sintering kinetics of thick thermal barrier coatings by thermal diffusivity measurements*, Journal of European Ceramic Society 25, **2005**, pp. 393-400.
31. Y. Tan, J.P. Longtin, and S. Sampath, *Effect of the Starting Microstructure on the Thermal Properties of As-Sprayed and Thermally Exposed Plasma-Sprayed YSZ Coatings*, Journal of the American Ceramic Society 92[3], **2009**, pp. 710-716.
32. F. Nakamori, Y. Ohishi, H. Muta, K. Kurosaki, K. Fukumoto, S. Yamanaka, *Mechanical and thermal properties of* $ZrSiO_4$, Journal of Nuclear Science and Technology 54[11], **2017**, pp. 1267-1273.